

Very-high- and ultrahigh-frequency electric-field detection using high angular momentum Rydberg states

Roger C. Brown^{1,2,*}, Baran Kayim¹, Michael A. Viray¹, Abigail R. Perry^{1,3},
 Brian C. Sawyer¹ and Robert Wyllie^{1,†}

¹*Georgia Tech Research Institute, Atlanta, Georgia 30332, USA*

²*NIST, 325 Broadway, Boulder, Colorado 80305, USA*

³*Quantinuum, 303 S. Technology Court, Broomfield, Colorado 80021, USA*



(Received 25 May 2022; revised 10 March 2023; accepted 14 April 2023; published 12 May 2023)

We demonstrate resonant detection of rf electric fields from 240 to 900 MHz (very high frequency to ultrahigh frequency) using electromagnetically induced transparency to measure orbital angular momentum $L = 3 \rightarrow L' = 4$ Rydberg transitions. These Rydberg states are accessible with three-photon infrared optical excitation. By resonantly detecting rf in the electrically small regime, these states enable a new class of atomic receivers. We find good agreement between measured spectra and predictions of quantum defect theory for principal quantum numbers $n = 45$ to 70. Using a superhetrodyne detection setup, we measure the noise floor at $n = 50$ to be $13 \mu\text{V}/(\text{m}\sqrt{\text{Hz}})$. Additionally, we utilize data and a numerical model incorporating a five-level master equation solution to estimate the fundamental sensitivity limits of our system.

DOI: [10.1103/PhysRevA.107.052605](https://doi.org/10.1103/PhysRevA.107.052605)

I. INTRODUCTION

Rydberg atoms were recently used to measure radio-frequency (rf) electric-field amplitude [1], polarization [2], phase [3,4], and angle of arrival [5]. The detected field amplitude is traceable to fundamental atomic structure and has led to an artifact-free paradigm in rf field calibrations [6–9]. Since the rf field sensing region is defined by laser-atom interaction volume, new opportunities in subwavelength rf field visualization have emerged [10,11]. Temporal modulation of the detected rf field has resulted in communication demonstrations of atomic reception using amplitude modulation (AM), frequency modulation (FM) [12–16], binary phase-shift keying, and quadrature amplitude modulation [17]. A previous study demonstrated that atomic receivers can operate non-resonantly in the electrically small regime [18]. In this case, the data switching rate was taken to be equal to the carrier frequency (dc to 30 MHz) and not resonant with nearby Rydberg transition frequencies (>10 GHz). In order for atomic receivers to be compatible with common broadcast technologies (AM and FM radio, television [19]), they must be able to operate with a tunable carrier frequency distinct from the data rate. For example, U.S. ultrahigh-frequency (UHF) television channels 14 through 89 [20] occupy a frequency band from 470 to 890 MHz (with 6 MHz allocated per channel).

Among the attractive properties of so-called Rydberg receivers is the fact that they are not subject to the Chu limit for electrically small antennas [21–23]. This stems from the difference in the underlying physical mechanism of rf reception between conducting antennas and atoms. The Chu limit states that the bandwidth W is constricted for electrically small pas-

sive conductor antennas, where the characteristic radius of the antenna is less than the wavelength of the rf field, $\ell_{\text{ant}} < \lambda_{\text{rf}}$. Specifically,

$$\frac{W_{\text{Chu}}}{f_0} \lesssim \frac{(2\pi \ell_{\text{ant}})^3}{\lambda_{\text{rf}}^3}, \quad (1)$$

where $f_0 = c/\lambda_{\text{rf}}$ is the carrier frequency and c is the speed of light in vacuum. For example, for a lossless electrically small classical antenna with $2\pi \ell_{\text{ant}}/\lambda_{\text{rf}} = 0.5$, the bandwidth is limited to $W/f_0 \lesssim 0.1$ [24].

In a typical Rydberg atomic receiver experiment [12–17], $f_0 \approx 10$ to 40 GHz, $W \lesssim 30$ MHz, and the optical path length in the atomic vapor is $0.5 < \ell_v < 10$ cm. To create an electrically small atomic receiver able to surpass a Chu-limited antenna in the 10 to 40 GHz range, atomic receiver bandwidth will need to be increased about 100-fold while reducing the apparatus size from centimeters to millimeters. However, at reduced carrier frequency, λ_{rf} becomes large such that $\ell_v \ll \lambda_{\text{rf}}$. For example, choosing $f_0 = 300$ MHz with typical atomic parameters ($W = 10$ MHz, $\ell_v \approx 3$ cm $< \lambda_{\text{rf}} = 1$ m) enables an electrically small receiver.

Here, we explore $nF_{7/2} \rightarrow nG_{9/2}$ Rydberg transitions in rubidium vapor with resonances from 240 to 900 MHz for very-high-frequency (VHF) to UHF rf detection. Two demonstrated approaches to reduce f_0 are (i) using nonresonant detection [25–28] and (ii) increasing the principal quantum number n of resonant detection [1]. In nonresonant detection schemes, the extension to low rf frequency requires that the amplitude of the detected field be large enough (volts to kilovolts per centimeter) to mix in nearby Rydberg states and can require the interpretation and simulation of Floquet spectra [26–28]. To maximize sensitivity to incident rf fields, we choose sensors where Autler-Townes (AT) [29] splitting of Rydberg states is resonantly detected

*roger.brown@nist.gov

†robert.wyllie@gtri.gatech.edu

with electromagnetically induced transparency (EIT) [30,31]. Resonant AT-EIT detection has been shown to sense rf fields with amplitudes near microvolts per centimeter at carrier frequencies defined by the difference in energy between Rydberg states [1,4,32]. Reducing f_0 requires optical excitation to higher Rydberg states that are increasingly susceptible to perturbation from other effects, e.g., dc Stark-induced state mixing and long-range Rydberg-Rydberg and Rydberg-ground-state collisions [33–35]. To our knowledge, the lowest published AT-EIT-detected rf signal is at 724 MHz, with $n > 130$ [7]. Higher angular momentum ($nF_{7/2} \rightarrow nG_{9/2}$) Rydberg transitions are more than an order of magnitude lower in energetic separation at a given principal quantum number compared to lower angular momentum transitions (see Fig. 3 below). Using these higher angular momentum states, we demonstrate resonant AT-EIT rf sensing with f_0 from 240 to 900 MHz using $n = 75$ to $n = 40$. Achieving $f_0 = 240$ MHz using the more familiar $nP_{3/2} \rightarrow (n-1)D_{5/2}$ transitions would require excitation to $n > 200$.

This paper is structured as follows: In Sec. II we present our experimental apparatus and present measurements of rf transitions between nF and nG . In Sec. III we present a numerical model, and in Sec. IV we use it to assess the sensitivity of the system to estimate the fundamental noise limits of our data. Finally, in Sec. V, we conclude with an outlook for future work.

II. EXPERIMENT

To access Rydberg states with orbital angular momentum, $L > 3$, we use the three-photon ladder system shown in Fig. 1(a). This ladder system was previously studied in a number of contexts, including fundamental atomic structure [36,37], rf field calibration in the 100-GHz range using both EIT and electromagnetically induced absorption [38], time-domain signal reception at 1.2 GHz [39], and quantum optics [40]. A variety of other multiphoton Rydberg excitation pathways have been explored [41–45]; however, none of them have been used to optically couple to $L \geq 3$ states [46]. This ladder system is appealing for a number of reasons. First, it utilizes transitions accessible by diode lasers. The two initial steps are also accessible by frequency-doubled telecom-band fiber lasers with a linewidth below the Rydberg-state linewidth. Second, the transition dipole moments between successive ladder states are larger than in one- or two-photon Rydberg excitation (increasing Rabi-excitation rates for fixed optical powers). Third, the near degeneracy in optical frequency between the first two steps in optical excitation allows access to a broader range of atomic velocity classes in a vapor cell [38,47].

The EIT probe laser beam addresses the $5S_{1/2}, F = 2 \rightarrow 5P_{3/2}, F' = 3$ transition at 780 nm. The effective Rydberg EIT coupling beam comprises a two-step optical excitation with a variable intermediate detuning from the $5D_{5/2}, F = 4$ state. The $5P_{3/2}, F = 3 \rightarrow 5D_{5/2}, F' = 4$ dressing transition is at 776 nm, and the $5D_{5/2}, F = 4 \rightarrow nF_{7/2}, F' = 5$ (or $nP_{3/2}, F' = 3$) coupling laser is tuned from 1260 to 1253 nm to access $n = 45$ to $n = 70$ Rydberg states. The intermediate detuning from the $5D_{5/2}$ state can be adjusted to trade the

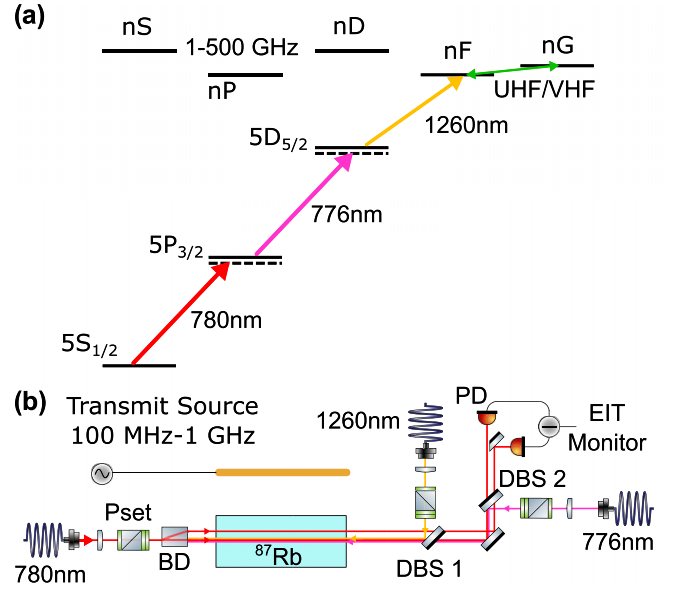


FIG. 1. (a) Level diagram for F -state Rydberg excitation and rf-induced Autler-Townes splitting in ^{87}Rb . Three electric dipole-allowed infrared transitions connect the ground state to the Rydberg $nF_{7/2}$ (or $nP_{3/2}$) states. Dashed virtual levels show the single-photon detunings of each step from atomic resonance. UHF to VHF fields, depicted with a green bidirectional arrow, can be detected via Autler-Townes splitting on the $nF \rightarrow nG$ Rydberg transitions, while 1 to 500 GHz can be detected on $nS \rightarrow nP$, $nP \rightarrow (n-1)D$, and $nF \rightarrow (n+1)D$ transitions. (b) Experimental schematic: the 780-nm probe beam counterpropagates in a Rb vapor cell with 776- and 1260-nm beams which form the effective EIT coupling beam. PD: photodiode; DBS: dichroic beam splitter; BD: beam displacer; Pset: polarization optics consisting of a $\lambda/2$ wave plate and a polarizing beam-splitter cube for power control followed by $\lambda/2$ and $\lambda/4$ wave plates for polarization control.

Rydberg excitation rate and intermediate-state-lifetime broadening effects.

The optical layout is shown in Fig. 1(b). Our rf sensing volume consists of a 75-mm-long, 19-mm-diameter cylindrical atomic vapor cell with a counterpropagating probe and dressing and coupling laser beams. The room-temperature quartz vapor cell is filled with isotopically pure (98%) ^{87}Rb and has wedged fused silica windows at an 11° angle with respect to the laser-beam propagation direction. After interacting with the atomic medium, the 780-nm probe beam is split from the 776- and 1260-nm beams and monitored with a photodiode.

The 780-, 776-, and 1260-nm beam waists ($1/e^2$ radius) are measured to be 587(60), 598(60), and 592(60) μm , with typical powers of 141(9) μW , 13.7(8) mW, and 233(14) mW, respectively. We estimate the upper bounds for optical excitation Rabi rates using the stretched-state dipole matrix elements to be $2\pi \times 17(3)$ MHz for the 780-nm transition, $2\pi \times 52(6)$ MHz for the 776-nm transition, and $2\pi \times 13(2)$ MHz ($2\pi \times 7(1)$ MHz) for the 1260-nm transition to $n = 45$ ($n = 70$) [34]. The 780- and 776-nm lasers are frequency stabilized to reference vapor cells using one- and two-color polarization-rotation spectroscopy [48,49], respectively. The probe laser is locked 10 MHz below the optical cycling $5S_{1/2}, F = 2 \rightarrow 5P_{3/2}, F = 3$ transition. The

intermediate-coupling laser is locked 30 MHz below the $5P_{3/2}F = 3 \rightarrow 5D_{5/2}F = 4$ transition. The 1260-nm laser can either be locked to a wavemeter or scanned across the three-photon resonance.

The 780-nm probe intensity is measured by a photodiode during a scan of the 1260-nm laser frequency across EIT resonance. To suppress probe-laser intensity noise, we can optionally use a reference probe beam without counterpropagating lasers and a differential photodetector [4,50]. To calibrate the 1260-nm laser frequency scan, we simultaneously record the transmission of a fiber-based Michelson interferometer with a free spectral range of 30(3) MHz, allowing frequency-scan nonlinearity to be removed in post-processing. The scan center frequency is recorded on a wavemeter with ± 50 -MHz accuracy. This wavemeter accuracy is sufficient to identify the principal quantum number of each Rydberg transition; it is not used to measure rf transition frequencies.

The source of rf radiation in our setup is a linear 17-cm monopole antenna connected to an rf synthesizer and placed roughly 20 cm away from the vapor cell. The cell and antenna are mounted 15 cm above an aluminum breadboard on a dielectric post. We expect nontrivial contributions from the breadboard to the overall radiation pattern of the antenna since the separation is smaller than the 33-cm to 1.5-m rf wavelengths investigated here.

When the resonant $nF \rightarrow nG$ rf radiation coupling strength exceeds the EIT linewidth, the EIT line splits into two Autler-Townes peaks. Figure 2(a) shows the AT splitting of the $50F \rightarrow 50G$ transition as a function of 1260-nm laser detuning, in good agreement with a five-level optical Bloch equation simulation of the spectrum (see Sec. IV for further discussion). The observed EIT linewidth is primarily due to power broadening associated with the dressing and coupling Rabi rates and detuning from the intermediate $D_{5/2}$ state. In Fig. 2(b) we plot the measured Autler-Townes-peak frequency splitting of the $50F \rightarrow 50G$ transition as a function of the applied UHF electric field. This shows the expected linear scaling, applicable for use as an rf power standard [1,7,9]. The rf electric field can be calculated as

$$|\vec{E}| = \frac{\hbar}{\mu_R} \Omega_{\text{RF}} \quad (2)$$

using measured AT splitting Ω_{RF} and the known transition dipole moment μ_R . The slope of Fig. 2(b) and the Rydberg transition dipole moment (for the $|m_J| = 1/2$ π transition of $50F \rightarrow 50G$, $\mu_R = 1858ea_0$ [34]) can be used to calibrate the apparatus calibration factor from the signal generator power P_s to the electric field in the atomic sample, $\xi = |E|P_s^{-1/2}$. This will be used in Sec. IV to evaluate the sensitivity of our system.

Figure 3 illustrates the >10 times reduction in carrier frequency (increase in wavelength) at a given n that can be attained by using transitions between higher ($L \geq 3$) angular momentum states. The experimentally measured resonant transition frequencies and uncertainties are shown in green. The measurements are in good agreement with carrier frequencies computed from the ^{85}Rb G -series quantum defect model [51–54] after mass scaling [55]. These quantum defect-derived carrier frequencies are shown as solid curves, with

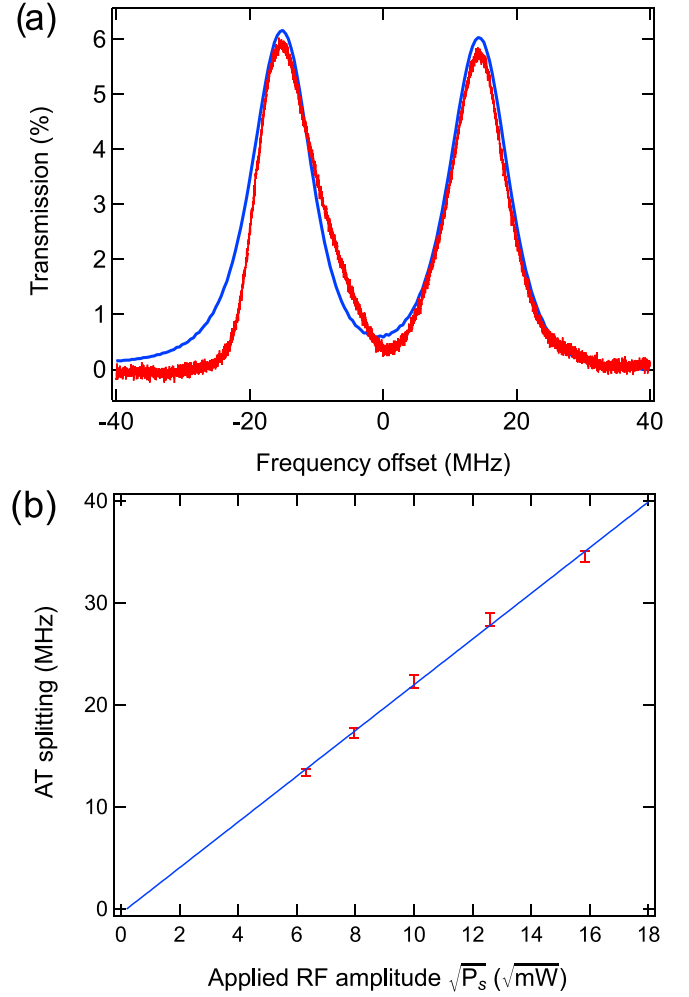


FIG. 2. (a) AT-EIT spectrum of the $50F \rightarrow 50G$ transition with an applied rf field of 655 MHz (red). A five-level simulated spectrum is underlaid by the data (blue). (b) Autler-Townes splitting of the $50F \rightarrow 50G$ EIT signal as a function of an applied UHF electric field. Point markers (red) are the measured uncertainties, with a linear fit to guide the eye (blue). This plot confirms the expected linear scaling between the rf electric field and Autler-Townes splitting.

the $nF_{7/2} \rightarrow nG_{9/2}$ transitions shown in green. The upper curves on this graph show resonant transition frequencies as a function of n for transitions with lower ($L \leq 3$) orbital angular momenta: $nS_{1/2} \rightarrow nP_{3/2}$, $nP_{3/2} \rightarrow (n-1)D_{5/2}$, and $nF_{7/2} \rightarrow (n+1)D_{5/2}$. These transitions were chosen because they have the largest dipole matrix elements and thus are the most sensitive for communications applications.

To determine the resonant Rydberg transition frequency in Fig. 3, we record the amplitude and separation of the Autler-Townes peaks as in Fig. 2(a). [56] On resonance, the amplitudes of the peaks are equal, and the separation between the two peaks is minimized. Off of resonance, the peak amplitudes become imbalanced, and the peak separation increases. The peak separations as a function of rf frequency reveal an approximately quadratic minimum about the rf carrier frequency. Spectra were recorded in a 30-MHz region approximately centered about the $nF \rightarrow nG$ transition frequency, with a frequency step size of 1 MHz. The peak positions

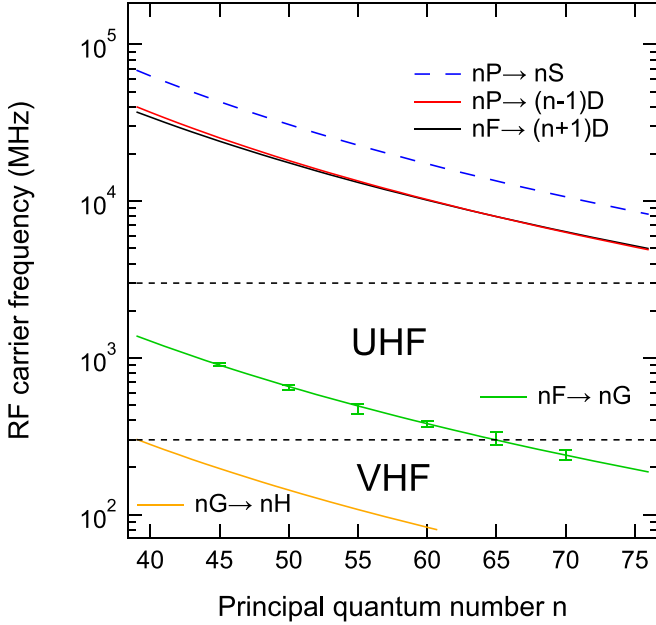


FIG. 3. The top three (blue dashed, red, and black) curves show calculated rf carrier frequencies [34] of commonly used lower angular momentum Rydberg states accessible by two-photon optical excitation. The middle (green) curve, located primarily in the UHF band, is the calculated rf carrier frequency associated with $nF_{7/2} \rightarrow nG_{9/2}$ transitions; the overlaid green point markers with uncertainty show corresponding measured carrier frequencies in the $n = 45$ to $n = 70$ range. The bottom (yellow) trace shows the calculated rf carrier frequency associated with $nG_{9/2} \rightarrow nH_{11/2}$ transitions.

are found by fitting independent Gaussian functions to each Autler-Townes peak. The peak separations are then fit to a quadratic to determine Rydberg resonance, with combined fit uncertainties of <24 MHz on average. We repeat this measurement for several principal quantum numbers in the $n = 45$ to $n = 70$ range.

For this measurement at $n = 70$, the vapor cell is more than an order of magnitude smaller than the rf wavelength ($\ell_{\text{vapor}}/\lambda_{\text{rf}} \approx 0.05$). Carrier frequencies may be further reduced using high angular momentum Rydberg states, and future experimental work will investigate the lower-frequency limits of this approach. For example, the $nG_{9/2} \rightarrow nH_{11/2}$ transitions, shown at the bottom of Fig. 3, are a factor of 4.6 lower in frequency at a given principal quantum number than the $nF_{7/2} \rightarrow nG_{9/2}$ transitions. These transitions can be accessed with additional rf fields. However, when the energetic spacing between transitions approaches the Rabi coupling rate (or, potentially, data bandwidth in communication applications) between the Rydberg states of interest, the incident rf will couple nearly resonantly to other higher L dipole-allowed transitions. This will result in complex spectra not easily interpreted for use in calibration or communication.

III. NUMERICAL MODEL

We develop a numerical model to benchmark our experimental data and compute fundamental sensitivity limits. We use a master-equation formalism to simulate the light-atom

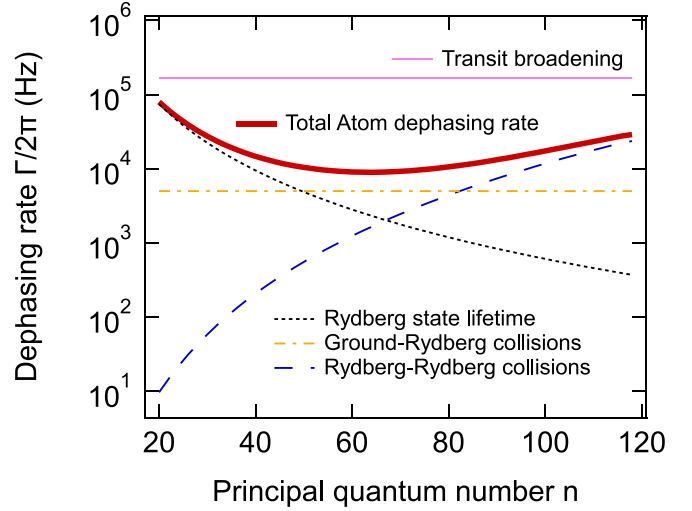


FIG. 4. Dephasing rates versus principal quantum number. Due to competing Rydberg state lifetime and collisional broadening effects, the atom-limited dephasing rate is minimized at intermediate principal quantum numbers $40 < n < 80$. This illustrates the advantage of decreasing rf carrier frequency by increasing L rather than increasing n . The traces in the legend have the same vertical ordering as the $n = 20$ data.

interaction, as in previous work [38,57,58]. We numerically compute the steady-state density matrix for the thermal ^{87}Rb sample. Our numerical model includes the experimental laser beam and rf intensities, propagation directions, polarizations, and frequency detunings from relevant Rb electronic transitions. We account for a number of state decay (T_1) and dephasing (T_2) processes via Lindblad operators [59]. These transition-broadening processes include finite laser linewidth, Rb state decay, transit broadening, and electronic-state-dependent collisional broadening (see Fig. 4). We model the system using five electronic states, $5S_{1/2}$, $5P_{3/2}$, $5D_{5/2}$, $nF_{7/2}$, and $nG_{9/2}$, while neglecting the full 45-level Zeeman structure for computational efficiency. The steady state is calculated for a range of atom velocities chosen from the Maxwell-Boltzmann distribution.

To account for collision-broadening effects, we calculate van der Waals (C_6) coefficients [60] for both Rydberg-Rydberg ($nF_{7/2}$ - $nF_{7/2}$ and $nF_{7/2}$ - $nG_{9/2}$) and $5S_{1/2}$ -Rydberg atomic collisions. We then use the eikonal approximation with the optical theorem [61] to calculate the total rate Γ_{SR} (Γ_{RR}) for $5S_{1/2}$ -Rydberg (Rydberg-Rydberg) collisions, as shown in Fig. 4. We include $5S_{1/2}$ -Rydberg collisional broadening using a phenomenological jump operator of the form $\Gamma_{SR}(|5S_{1/2}\rangle\langle R| + |R\rangle\langle 5S_{1/2}|)$, where $|R\rangle$ is the relevant Rydberg state.

We calculate a transit-broadening rate coefficient as the inverse of the average laser-beam transit time using vapor-cell temperature $T = 300$ K and the beam waists and generate a corresponding Lindblad operator by summing the outer products of each state vector with the ground state to indicate a T_1 decay. Similarly, we include Lindblad operators for the laser linewidth broadening and the various atomic state lifetimes. The magnitude of each dephasing rate is represented in Fig. 4, in addition to a “total-atom” dephasing rate, which is the sum

of all of the non-laser-dependent atomic broadening effects (collisions and Rydberg-state lifetime). The remaining broadening not included in this model may be due to electric-field inhomogeneity in the applied rf or a nonuniform distribution of metallic rubidium within the vapor cell along the axis of beam propagation. Figure 4 shows two atomic structure limitations to coherence time. At a low principal quantum number short atomic lifetimes dominate, while at a high principal quantum number Rydberg-Rydberg collisions dominate. The atom-limited dephasing rate is therefore minimized at intermediate principal quantum numbers $40 < n < 80$. This optimal atom-limited sensitivity again supports the choice to use $L \geq 3$ states to achieve lower rf carrier frequencies rather than simply going to higher n states.

For a comparison with absorption measurements, we compute the detuning-dependent optical absorption coefficient α experienced by the 780-nm probe laser beam as [38]

$$\alpha = \frac{2k_p n_V \epsilon \mu_p}{\epsilon_0 E_p}, \quad (3)$$

where

$$\epsilon = \int_{-\infty}^{\infty} P(v_x) \text{Im}(\rho_{01}) dv_x \quad (4)$$

is the atomic excitation fraction obtained via integration of the velocity-dependent quantity $\text{Im}(\rho_{01})$ weighted by the Maxwell-Boltzmann velocity distribution along the beam propagation direction, $P(v_x) = \sqrt{\frac{m}{2\pi kT}} \exp(-\frac{mv_x^2}{2kT})$. In Eq. (3), k_p is the probe-laser k -vector magnitude, E_p is the probe-laser electric field, n_V is the volumetric number density of ^{87}Rb atoms in the cell, μ_p is the electric dipole moment of the $5S_{1/2} \rightarrow 5P_{3/2}$ probe transition, and ϵ_0 is the permittivity of vacuum. Finally, we compute the fractional probe-laser-beam transmission as $\exp(-\alpha \ell_v)$.

IV. SENSITIVITY ASSESSMENT

We characterize the sensitivity of our system using the $50F \rightarrow 50G$ transition. Experimentally, we implement superheterodyne detection [3,4] using two rf fields: a signal field $E_s \cos[(\omega_{\text{LO}} + \delta)t]$ and a local oscillator $E_{\text{LO}} \cos(\omega_{\text{LO}}t - \phi_{\text{LO}})$. We first make a series of calibration measurements to obtain ξ [Fig. 2(b)], relating the signal generator power setting P_s to the electric field through Eq. (2) and $\xi = |E|P_s^{-1/2}$. We choose $\Omega_{\text{LO}} \approx \Gamma$ to bias the sensor to maximum sensitivity [60] and apply a calibrated signal field $E_s \ll E_{\text{LO}}$. When $\delta \ll \omega_{\text{LO}}$ and δ is within the atomic response bandwidth, the time-dependent atomic response is $E_s/2 \cos(\delta t + \phi_{\text{LO}})$ [62]. The beat-note amplitude then serves to calibrate the receiver response χ between the photodiode voltage and signal field E_s . We measure an amplitude spectral density noise floor of $E_n = 13(2) \mu\text{V}/(\text{m}\sqrt{\text{Hz}})$ for the $50F$ - $50G$ transition. The LO parameters are $E_{\text{LO}} = 0.37 \text{ V/m}$ (corresponding to $\Omega_{\text{LO}}/2\pi = 9.5 \text{ MHz}$) at $\omega_{\text{LO}}/2\pi = 655 \text{ MHz}$. The signal-field parameters are $E_s = 9.3 \text{ mV/m}$, with $\delta/2\pi = 50 \text{ kHz}$. Both fields are applied via the same rf horn. Figure 5 compares this calibrated amplitude spectral density with those of only the probe (without the dressing or coupling lasers) and the electronic noise floor without the probe. We find the noise dominated by

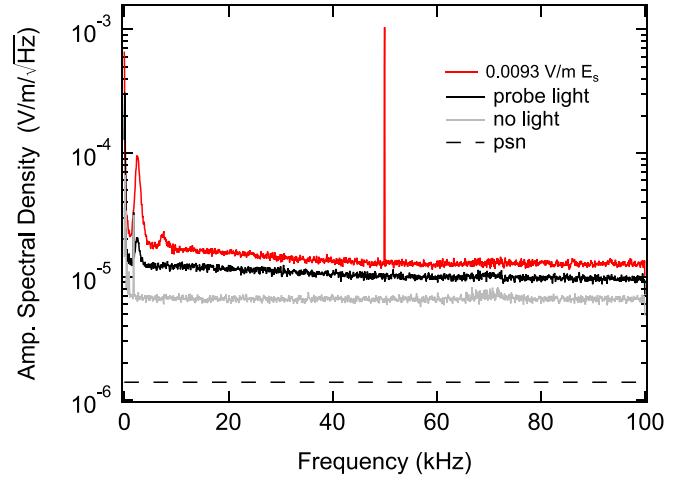


FIG. 5. Amplitude spectral density noise measurements at $n = 50$, $f_{\text{rf}} = 655 \text{ MHz}$ utilizing a superheterodyne technique and the parameters described in the text. The traces in the legend have the same vertical ordering as the data. The top red trace shows the noise with a 9.3 mV/m calibration field on, with a $13 \mu\text{V}/(\text{m}\sqrt{\text{Hz}})$ white-noise floor near the calibration frequency offset of 50 kHz from the LO field. The calibrated noise with only probe light (black solid trace) and without any light (light gray trace) and the photon shot noise (psn; black dashed trace) are shown for reference. The estimated quantum projection noise is $34 \text{ nV}/(\text{m}\sqrt{\text{Hz}})$, well below the range displayed.

probe detection and well above the photon shot-noise floor, indicating room for further improvement.

The fundamental sensitivity limits of Rydberg vapor quantum sensors are determined by the quantum projection noise and the photon shot noise [63]. Below, we utilize our model and measurements to estimate the applicable limits to our system in the UHF frequency range investigated here.

The quantum projection noise limited sensitivity to an rf electric-field amplitude E_{qpn} is

$$E_{\text{qpn}} = \frac{\hbar}{\mu_R} \frac{1}{\sqrt{NT_2t}}, \quad (5)$$

for the coherence time T_2 and t is the total measurement time. The number of atoms participating in the measurement is $N = \epsilon n_V V$ for an interaction volume defined by optical beam geometry $V = \pi w_0^2 \ell_{\text{eff}}$ for beam waists w_0 and effective interaction length ℓ_{eff} . Typical parameters in our simulations yield $10^{-3} < \epsilon < 10^{-2}$, significantly less than an estimation based on all available atoms in the laser-beam column [63,64]. At principal $n = 50$ at room temperature and with the experimental parameters defined above, we estimate $\epsilon = 10.7 \times 10^{-3}$ and participating atom number $N \sim 10^6$. We use the bare EIT FWHM $\Gamma = 2\pi \times 9.7 \text{ MHz}$ to estimate $T_2 = \Gamma^{-1}$ [4] and $\Delta E_{\text{qpn}} = 38 \text{ nV}/(\text{m}\sqrt{\text{Hz}})$.

The photon shot noise for a single photodiode intensity measurement is $\Delta I_{\text{psn}} = \sqrt{2e(\eta e \Phi_p) \Delta f}$, where e is the electron charge, η is the photodiode quantum efficiency, Φ_p is the probe photon flux incident upon the photodiode, and Δf is the measurement bandwidth [32]. Using the transimpedance amplifier gain G_v and the receiver response χ in photodiode response amps per applied E_{sig} , we can express this as a field

sensitivity limit,

$$\Delta E_{\text{psn}} = G_v \chi \Delta I_{\text{psn}}. \quad (6)$$

The photon shot noise in Fig. 5 is $\Delta E_{\text{psn}} = 1.6 \mu\text{V}/(\text{m}\sqrt{\text{Hz}})$, a factor of 40 higher than E_{qpn} . Technical improvements that will be pursued in future work to reach the photon shot-noise limit include intensity stabilization and the addition of a laser to repump the ground-state population [50] and, potentially, comb-based optical probing [65].

V. OUTLOOK

We have demonstrated AT-EIT rf field sensitivity using $nF \rightarrow nG$ Rydberg transitions that enable resonant electrically small UHF receivers. Future work includes recording temporally modulated fields to characterize the sensitivity and bandwidth at UHF and lower frequencies. This can be done by using portable laser systems and operating in a controlled rf environment since λ_{rf} is comparable to or larger than many optical elements. Furthermore, this approach is compatible

with using auxiliary rf fields to Stark-tune the desired rf frequency [57,66], offering continuous tuning between atomic transitions.

The three-photon all-infrared optical excitation approach also offers a number of benefits that may be further explored. The three optical beams may be aligned in a planar orientation to achieve Doppler-free and recoil-free excitation [67–69], potentially enabling Rydberg lifetime-limited narrow spectral features useful in precise rf field calibrations. Infrared optical excitation may also enable simplified all-dielectric vapor-cell sensor heads with more uniformly applied EIT coupling fields compared to infrared-blue excitation [70]. This should reduce transit broadening and increase sensitivity in a deployable package.

ACKNOWLEDGMENTS

We thank V. Gerginov, R. Westafer, C. D. Herold, and M. Lombardi for comments and careful reading of the manuscript. We acknowledge funding from the Air Force Research Laboratory (Release Approval No. AFRL-2022-1980) and the GTRI HIVES program.

-
- [1] J. A. Sedlacek, A. Schwettmann, H. Kübler, R. Löw, T. Pfau, and J. P. Shaffer, Microwave electrometry with Rydberg atoms in a vapour cell using bright atomic resonances, *Nat. Phys.* **8**, 819 (2012).
 - [2] J. A. Sedlacek, A. Schwettmann, H. Kübler, and J. P. Shaffer, Atom-Based Vector Microwave Electrometry Using Rubidium Rydberg Atoms in a Vapor Cell, *Phys. Rev. Lett.* **111**, 063001 (2013).
 - [3] M. T. Simons, A. H. Haddab, J. A. Gordon, and C. L. Holloway, A Rydberg atom-based mixer: Measuring the phase of a radio frequency wave, *Appl. Phys. Lett.* **114**, 114101 (2019).
 - [4] M. Jing, Y. Hu, J. Ma, H. Zhang, L. Zhang, L. Xiao, and S. Jia, Atomic superheterodyne receiver based on microwave-dressed Rydberg spectroscopy, *Nat. Phys.* **16**, 911 (2020).
 - [5] A. K. Robinson, N. Prajapati, D. Senic, M. T. Simons, and C. L. Holloway, Determining the angle-of-arrival of a radio-frequency source with a Rydberg atom-based sensor, *Appl. Phys. Lett.* **118**, 114001 (2021).
 - [6] E. A. Donley, T. Crowley, T. P. Heaven, and B. Riddle, A quantum-based microwave power measurement performed with a miniature atomic fountain, in *Proceedings of the 2003 IEEE International Frequency Control Symposium and PDA Exhibition Jointly with the 17th European Frequency and Time Forum, 2003* (IEEE, Piscataway, NJ, 2003), pp. 135–137.
 - [7] C. L. Holloway, M. T. Simons, J. A. Gordon, P. F. Wilson, C. M. Cooke, D. A. Anderson, and G. Raithel, Atom-based RF electric field metrology: From self-calibrated measurements to sub-wavelength and near-field imaging, *IEEE Trans. Electromagn. Compat.* **59**, 717 (2017).
 - [8] C. L. Holloway, M. T. Simons, J. A. Gordon, A. Dienstfrey, D. A. Anderson, and G. Raithel, Electric field metrology for SI traceability: Systematic measurement uncertainties in electromagnetically induced transparency in atomic vapor, *J. Appl. Phys.* **121**, 233106 (2017).
 - [9] S. Chen, D. J. Reed, A. R. MacKellar, L. A. Downes, N. F. A. Almuhawish, M. J. Jamieson, C. S. Adams, and K. J. Weatherill, Terahertz electrometry via infrared spectroscopy of atomic vapor, *Optica* **9**, 485 (2022).
 - [10] H. Q. Fan, S. Kumar, R. Daschner, H. Kübler, and J. P. Shaffer, Subwavelength microwave electric-field imaging using Rydberg atoms inside atomic vapor cells, *Opt. Lett.* **39**, 3030 (2014).
 - [11] C. L. Holloway, M. T. Simons, M. D. Kautz, A. H. Haddab, J. A. Gordon, and T. P. Crowley, A quantum-based power standard: Using Rydberg atoms for a Si-traceable radio-frequency power measurement technique in rectangular waveguides, *Appl. Phys. Lett.* **113**, 094101 (2018).
 - [12] D. H. Meyer, K. C. Cox, F. K. Fatemi, and P. D. Kunz, Digital communication with Rydberg atoms and amplitude-modulated microwave fields, *Appl. Phys. Lett.* **112**, 211108 (2018).
 - [13] Z. Song, H. Liu, X. Liu, W. Zhang, H. Zou, J. Zhang, and J. Qu, Rydberg-atom-based digital communication using a continuously tunable radio-frequency carrier, *Opt. Express* **27**, 8848 (2019).
 - [14] D. A. Anderson, R. E. Sapiro, and G. Raithel, An atomic receiver for am and fm radio communication, *IEEE Trans. Antennas Propag.* **69**, 2455 (2021).
 - [15] A. B. Deb and N. Kjærgaard, Radio-over-fiber using an optical antenna based on Rydberg states of atoms, *Appl. Phys. Lett.* **112**, 211106 (2018).
 - [16] D. A. Anderson, R. E. Sapiro, and G. Raithel, Rydberg atoms for radio-frequency communications and sensing: Atomic receivers for pulsed rf field and phase detection, *IEEE Aerospace Electron. Syst. Mag.* **35**, 48 (2020).
 - [17] C. L. Holloway, M. T. Simons, J. A. Gordon, and D. Novotny, Detecting and receiving phase-modulated signals with a Rydberg atom-based receiver, *IEEE Antennas Wireless Propag. Lett.* **18**, 1853 (2019).

- [18] K. C. Cox, D. H. Meyer, F. K. Fatemi, and P. D. Kunz, Quantum-Limited Atomic Receiver in the Electrically Small Regime, *Phys. Rev. Lett.* **121**, 110502 (2018).
- [19] N. Prajapati, A. P. Rotunno, S. Berweger, M. T. Simons, A. B. Artusio-Glimpse, S. D. Voran, and C. L. Holloway, TV and video game streaming with a quantum receiver: A study on a Rydberg atom-based receiver's bandwidth and reception clarity, *AVS Quantum Sci.* **4**, 035001 (2022).
- [20] National Telecommunications and Information Administration, Tables of frequency allocations, <https://www.ntia.doc.gov/legacy/osmhome/alloctbl/allocmhz.html>.
- [21] L. J. Chu, Physical limitations of omni-directional antennas, *J. Appl. Phys.* **19**, 1163 (1948).
- [22] H. Wheeler, Fundamental limitations of small antennas, *Proc. IRE* **35**, 1479 (1947).
- [23] R. F. Harrington, Effect of antenna size on gain, bandwidth, and efficiency, *J. Res. Natl. Bur. Stand.* **64**, 1 (1960).
- [24] D. F. Sievenpiper, D. C. Dawson, M. M. Jacob, T. Kanar, S. Kim, J. Long, and R. G. Quarfoth, Experimental validation of performance limits and design guidelines for small antennas, *IEEE Trans. Antennas Propag.* **60**, 8 (2012).
- [25] M. G. Bason, M. Tanasittikosol, A. Sargsyan, A. K. Mohapatra, D. Sarkisyan, R. M. Potvliege, and C. S. Adams, Enhanced electric field sensitivity of rf-dressed Rydberg dark states, *New J. Phys.* **12**, 065015 (2010).
- [26] S. A. Miller, D. A. Anderson, and G. Raithel, Radio-frequency-modulated Rydberg states in a vapor cell, *New J. Phys.* **18**, 053017 (2016).
- [27] Y. Jiao, L. Hao, X. Han, S. Bai, G. Raithel, J. Zhao, and S. Jia, Atom-Based Radio-Frequency Field Calibration and Polarization Measurement Using Cesium nD_J Floquet States, *Phys. Rev. Appl.* **8**, 014028 (2017).
- [28] E. Paradis, G. Raithel, and D. A. Anderson, Atomic measurements of high-intensity VHF-band radio-frequency fields with a Rydberg vapor-cell detector, *Phys. Rev. A* **100**, 013420 (2019).
- [29] S. H. Autler and C. H. Townes, Stark effect in rapidly varying fields, *Phys. Rev.* **100**, 703 (1955).
- [30] A. K. Mohapatra, T. R. Jackson, and C. S. Adams, Coherent Optical Detection of Highly Excited Rydberg States Using Electromagnetically Induced Transparency, *Phys. Rev. Lett.* **98**, 113003 (2007).
- [31] K.-J. Boller, A. Imamoglu, and S. E. Harris, Observation of Electromagnetically Induced Transparency, *Phys. Rev. Lett.* **66**, 2593 (1991).
- [32] S. Kumar, H. Fan, H. Kübler, A. J. Jahangiri, and J. P. Shaffer, Rydberg-atom based radio-frequency electrometry using frequency modulation spectroscopy in room temperature vapor cells, *Opt. Express* **25**, 8625 (2017).
- [33] T. F. Gallagher, *Rydberg Atoms* (Cambridge University Press, Cambridge, 1994).
- [34] N. Ćibalić, J. Pritchard, C. Adams, and K. Weatherill, Arc: An open-source library for calculating properties of alkali Rydberg atoms, *Comput. Phys. Commun.* **220**, 319 (2017).
- [35] E. Robertson, N. Ćibalić, R. Potvliege, and M. Jones, Arc 3.0: An expanded python toolbox for atomic physics calculations, *Comput. Phys. Commun.* **261**, 107814 (2021).
- [36] P. Thoumany, T. Germann, T. Hänsch, G. Stania, L. Urbonas, and T. Becker, Spectroscopy of rubidium Rydberg states with three diode lasers, *J. Mod. Opt.* **56**, 2055 (2009).
- [37] L. A. M. Johnson, H. O. Majeed, B. Sanguinetti, T. Becker, and B. T. H. Varcoe, Absolute frequency measurements of $^{85}\text{Rb } nF_{7/2}$ Rydberg states using purely optical detection, *New J. Phys.* **12**, 063028 (2010).
- [38] N. Thaicharoen, K. R. Moore, D. A. Anderson, R. C. Powell, E. Peterson, and G. Raithel, Electromagnetically induced transparency, absorption, and microwave-field sensing in a Rb vapor cell with a three-color all-infrared laser system, *Phys. Rev. A* **100**, 063427 (2019).
- [39] S. H. You, M. H. Cai, S. S. Zhang, Z. S. Xu, and H. P. Liu, Microwave-field sensing via electromagnetically induced absorption of Rb irradiated by three-color infrared lasers, *Opt. Express* **30**, 16619 (2022).
- [40] O. Lahad, R. Finkelstein, O. Davidson, O. Michel, E. Poem, and O. Firstenberg, Recovering the Homogeneous Absorption of Inhomogeneous Media, *Phys. Rev. Lett.* **123**, 173203 (2019).
- [41] C. Carr, M. Tanasittikosol, A. Sargsyan, D. Sarkisyan, C. S. Adams, and K. J. Weatherill, Three-photon electromagnetically induced transparency using Rydberg states, *Opt. Lett.* **37**, 3858 (2012).
- [42] L.-H. Zhang, Z.-K. Liu, B. Liu, Z.-Y. Zhang, G.-C. Guo, D.-S. Ding, and B.-S. Shi, Rydberg Microwave-Frequency-Comb Spectrometer, *Phys. Rev. Appl.* **18**, 014033 (2022).
- [43] J. M. Kondo, N. Šibalić, A. Guttridge, C. G. Wade, N. R. D. Melo, C. S. Adams, and K. J. Weatherill, Observation of interference effects via four-photon excitation of highly excited Rydberg states in thermal cesium vapor, *Opt. Lett.* **40**, 5570 (2015).
- [44] J. Shaffer and H. Kübler, A read-out enhancement for microwave electric field sensing with Rydberg atoms, in *Quantum Technologies 2018*, edited by J. Stuhler, A. J. Shields, and M. J. Padgett, International Society for Optics and Photonics, Vol. 10674 (SPIE, 2018), p. 106740C.
- [45] J. Bai, Y. Jiao, Y. He, R. Song, J. Zhao, and S. Jia, Autler-Townes splitting of three-photon excitation of cesium cold Rydberg gases, *Opt. Express* **30**, 16748 (2022).
- [46] This is often because it is either technologically or scientifically attractive for the second leg of the ladder to connect $P \rightarrow S$ states.
- [47] Access to the largest number of atomic velocity classes occurs when the 780-nm beam counter propagates with the 776- and 1260-nm beams and with a small frequency offset from the $5D_{5/2}$ state, creating stronger spectral features in room-temperature atomic vapors than in other three-photon excitation schemes.
- [48] C. Wieman and T. W. Hänsch, Doppler-Free Laser Polarization Spectroscopy, *Phys. Rev. Lett.* **36**, 1170 (1976).
- [49] C. Carr, C. S. Adams, and K. J. Weatherill, Polarization spectroscopy of an excited state transition, *Opt. Lett.* **37**, 118 (2012).
- [50] N. Prajapati, A. K. Robinson, S. Berweger, M. T. Simons, A. B. Artusio-Glimpse, and C. L. Holloway, Enhancement of electromagnetically induced transparency based Rydberg-atom electrometry through population repumping, *Appl. Phys. Lett.* **119**, 214001 (2021).
- [51] J. Han, Y. Jamil, D. V. L. Norum, P. J. Tanner, and T. F. Gallagher, Rb nf quantum defects from millimeter-wave spectroscopy of cold ^{85}Rb Rydberg atoms, *Phys. Rev. A* **74**, 054502 (2006).

- [52] K. Afrousheh, P. Bohlouli-Zanjani, J. A. Petrus, and J. D. D. Martin, Determination of the ^{85}Rb ng -series quantum defect by electric-field-induced resonant energy transfer between cold Rydberg atoms, *Phys. Rev. A* **74**, 062712 (2006).
- [53] L. A. M. Johnson, Precision laser spectroscopy of Rubidium with a frequency comb, Ph.D. thesis, University of Leeds, Leeds, 2011.
- [54] K. Moore, A. Duspayev, R. Cardman, and G. Raithel, Measurement of the Rb g -series quantum defect using two-photon microwave spectroscopy, *Phys. Rev. A* **102**, 062817 (2020).
- [55] The isotope shift between values for ^{85}Rb and the data measured here for ^{87}Rb is accounted for by mass scaling the infinite-nuclear-mass Rydberg constant $R_\infty = (e^4 m_e)/(16\pi^2 \epsilon_0^2 \hbar^2)$ (here, e is the electron charge, m_e is the mass of the electron) by the factor $R_n = R_\infty \times M_n/(M_n + m_e)$ (M_n is the mass of the atomic nucleus) not by adjusting the quantum defects.
- [56] For the data shown in Fig. 3, the 780-, 776-, and 1260-nm beam waists ($1/e^2$) are measured to be 55(6), 55(6), and 65(7) μm , with typical powers of 4(0.3) μW , 130(8) μW , and 40(3) mW, respectively.
- [57] M. T. Simons, A. B. Artusio-Glimpse, C. L. Holloway, E. Imhof, S. R. Jefferts, R. Wyllie, B. C. Sawyer, and T. G. Walker, Continuous radio-frequency electric-field detection through adjacent Rydberg resonance tuning, *Phys. Rev. A* **104**, 032824 (2021).
- [58] S. N. Sandhya and K. K. Sharma, Atomic coherence effects in four-level systems: Doppler-free absorption within an electromagnetically-induced-transparency window, *Phys. Rev. A* **55**, 2155 (1997).
- [59] D. Manzano, A short introduction to the Lindblad master equation, *AIP Adv.* **10**, 025106 (2020).
- [60] H. Q. Fan, S. Kumar, S. Sedlacek, H. Kübler, S. Karimkashi, and J. P. Shaffer, Atom based rf electric field sensing, *J. Phys. B* **48**, 202001 (2015).
- [61] J. J. Sakurai, *Modern Quantum Mechanics*, rev. ed., edited by S. F. Tuan (American Association of Physics Teachers, San Francisco, 1995).
- [62] D. H. Meyer, P. D. Kunz, and K. C. Cox, Waveguide-Coupled Rydberg Spectrum Analyzer from 0 to 20 GHz, *Phys. Rev. Appl.* **15**, 014053 (2021).
- [63] D. H. Meyer, C. O'Brien, D. P. Fahey, K. C. Cox, and P. D. Kunz, Optimal atomic quantum sensing using electromagnetically-induced-transparency readout, *Phys. Rev. A* **104**, 043103 (2021).
- [64] D. H. Meyer, Z. A. Castillo, K. C. Cox, and P. D. Kunz, Assessment of Rydberg atoms for wideband electric field sensing, *J. Phys. B* **53**, 034001 (2020).
- [65] K. Dixon, K. Nickerson, D. W. Booth, and J. P. Shaffer, Rydberg-Atom-Based Electrometry Using a Self-Heterodyne Frequency-Comb Readout and Preparation Scheme, *Phys. Rev. Appl.* **19**, 034078 (2023).
- [66] T. Vogt, C. Gross, T. F. Gallagher, and W. Li, Microwave-assisted Rydberg electromagnetically induced transparency, *Opt. Lett.* **43**, 1822 (2018).
- [67] G. Grynberg, F. Biraben, M. Bassini, and B. Cagnac, Three-Photon Doppler-Free Spectroscopy: Experimental Evidence, *Phys. Rev. Lett.* **37**, 283 (1976).
- [68] I. I. Ryabtsev, I. I. Beterov, D. B. Tretyakov, V. M. Entin, and E. A. Yakshina, Doppler- and recoil-free laser excitation of Rydberg states via three-photon transitions, *Phys. Rev. A* **84**, 053409 (2011).
- [69] N. Šibalić, J. M. Kondo, C. S. Adams, and K. J. Weatherill, Dressed-state electromagnetically induced transparency for light storage in uniform-phase spin waves, *Phys. Rev. A* **94**, 033840 (2016).
- [70] M. T. Simons, J. A. Gordon, and C. L. Holloway, Fiber-coupled vapor cell for a portable Rydberg atom-based radio frequency electric field sensor, *Appl. Opt.* **57**, 6456 (2018).